Friction **11**(7): 1253–1264 (2023)
https://doi.org/10.1007/s40544-022-0658-x
ISSN 2223-7690
CN 10-1237/TH

RESEARCH ARTICLE

Application of physics-informed neural network in the analysis of hydrodynamic lubrication

Yang ZHAO[1,*], **Liang GUO**[2], **Patrick Pat Lam WONG**[3]

[1] *School of Automotive and Transportation Engineering, Shenzhen Polytechnic, Shenzhen 518055, China*

[2] *School of Mechatronic Engineering and Automation, Shanghai University, Shanghai 200444, China*

[3] *Department of Mechanical Engineering, City University of Hong Kong, Hong Kong, China*

Received: 20 December 2021 / Revised: 28 January 2022 / Accepted: 23 May 2022

Abstract: The last decade has witnessed a surge of interest in artificial neural network in many different areas of scientific research. Despite the rapid expansion in the application of neural networks, few efforts have been carried out to introduce such a powerful tool into lubrication studies. Thus, this work aims to apply the physics-informed neural network (PINN) to the hydrodynamic lubrication analysis. The 2D Reynolds equation is solved. The PINN is a meshless method and does not require big data for network training compared with classical methods. Our results are consistent with those obtained by experiments and the finite element method. Hence, we envision that the PINN method will have great application potential in lubrication and bearing research.

Keywords: physics-informed neural network; hydrodynamic lubrication; slider bearing

1 Introduction

Effective hydrodynamic lubrication plays a crucial role in bearing performance [1]. The hydrodynamics of lubricants in bearings is governed by the Reynolds equation. Hence, its accurate solution paves the critical foundation that supports the realisation of different types of bearings and contributes to almost every aspect in engineering lubrication [1]. The 1D Reynolds equation appears to be a simple form that assumes uniform pressure distribution (i.e., zero pressure gradient) across the entrainment direction and can be readily analytically solved [2]. Gohar and Safa [2] derived an analytical expression of the pressure distribution from the 1D Reynolds equation. However, the 1D Reynolds equation is only valid for bearings of infinite width, where the width B of the bearing (across the entrainment direction) is at least 3 times greater than its length L (in the entrainment direction) [2]. The 2D Reynolds equation must be solved to account for the side-leakage in bearings of finite width, such as slider bearings [3]. Although the 2D Reynolds equation has no analytical solution, researchers managed to solve it by numerical methods, such as the finite difference [4], finite volume [5], or finite element (FEM) [6] methods. These numerical methods rely on grid discretisation [7] and have been proven to be effective for lubrication analysis. However, few of these methods are able to take full advantage of modern technologies, such as artificial neural network [8] and machine learning [9], which have already been applied in various areas of engineering research [8–10].

Recently, advances in neural networks have stridden ahead and brought their impact to the edge of tribology research [11]. Zhang et al. [12] adopted the neural network to predict the wear loss of bushings in the variable stator vane assemblies and achieved more than 90% accuracy rate in the prediction of wear loss. Canbulut et al. [13] designed a simple

* Corresponding author: Yang ZHAO, E-mail: yzhao84-c@my.cityu.edu.hk

Nomenclature

b	Bias of neuron	p	Pressure (Pa)
B	Bearing width (m)	P	Dimensionless pressure ($P = ph_0^2/(U\eta L)$)
$C(\boldsymbol{w})$	Loss during training	U	Sliding velocity (m/s)
h	Film thickness (m)	W	Applied load (N)
h_0	Outlet film thickness (m)	z	Neuron output
H	Dimensionless film thickness ($H = h/h_o$)	$\boldsymbol{\lambda}$	Working condition vector
L	Bearing length (m)	η	Lubricant viscosity ($\mathrm{Pa}\cdot\mathrm{s}$)
$N[X,Y]^T$	Neural network	θ	Inclination
N_e	Maximum allowable epoch number	$\phi(\xi)$	Activation function
N_L	Layer number	w	Weight of neuron
N_n	Neuron number of each layer	Ω_L	Lubrication domain

feedforward neural network to predict the frictional power loss in the hydrostatic bearings. The predicted power loss greatly correlated with the experimental measurements. In contrast with the conventional method for friction prediction, the constructed neural network [13] is able to simultaneously process multiple inputs, such as surface roughness and sliding velocity. Perčić et al. [14] presented a new method for friction prediction at nanoscale by mapping the input–output patterns with machine learning and forecasting the friction through data processing. They also adopted the artificial intelligence model to generate mathematical expressions for friction prediction. Sadegh et al. [15] combined the back-propagation neural network and generic algorithm to analyse the frequencies of measured signals, such that the different lubrication states of journal bearings, namely, hydrodynamic, mixed and boundary, could be distinguished.

Although the neural network technology has extended the frontiers of tribology research, classical neural networks require large data sets for neural network training. This requirement largely limits their application potential. To overcome this drawback, Raissi et al. [16] devised a physics-informed neural network (PINN) to solve the partial differential equations (PDEs) by leveraging the universal approximating ability of neural networks [17]. They exploited automatic differentiation tools in neural networks to obtain the derivatives in the PDEs and converted the PDEs into PINNs. Accordingly, they enabled the use of the state-of-the-art neural network technology to construct PINN. Other than the boundary and initial values of PDEs, the PINN does not need any extra data for neural network training. Substantial comparison of the results predicted by PINN and other methods clearly confirmed the effectiveness of PINN as an alternative solver for PDEs. Samaniego et al. [18] have recently developed a similar approach, namely deep energy method (DEM), that employs the potential energy of the system as the loss function to construct the neural network. They have successfully analysed various mechanical and electro-mechanical problems using the newly devised DEM neural network. Subsequently, Nguyen-Thanh et al. [19] have updated DEM by incorporating the concept of FEM domain-mapping. The original computational domain is mapped into a regulated parametric domain (e.g., square) to enable the general solution of problems defined in complicated domains. They have successfully applied their method to the strain gradient problems, which are not easily solved by the classical FEM. Recently, Almqvist [20] implemented the PINN method to tackle the 1D Reynolds equation. The pressure predicted by PINN corresponds well with that calculated by analytical expressions. According to Zubov et al. [8] and Almqvist [20], PINN has the merit of being a meshless method, which overcomes the "curse of dimension" [21] that the classical methods, such as FEM, face.

Herein, we extend the work of Almqvist [20] to solve the 2D Reynolds equation using the PINN method for the hydrodynamic lubrication analysis of

a slider bearing. The PINN method is applied to the iterative solution process for the pressure and film thickness distributions in the analysis. The influences of epoch, layer, and neuron numbers of PINN on the accuracy of the predicted pressure distribution are discussed.

2 PINN architecture

This work focuses on investigating the lubrication conditions in the hydrodynamic lubrication contacts, where the dimensionless form of Reynolds equation is

$$\mathrm{Rey}\left(P,X,Y;\boldsymbol{\lambda}\right)=\frac{\partial}{\partial X}\left(H^3\frac{\partial P}{\partial X}\right)+\frac{L^2}{B^2}\frac{\partial}{\partial Y}\left(H^3\frac{\partial P}{\partial Y}\right)-6\frac{\partial H}{\partial X}=0 \tag{1}$$

where P is the dimensionless pressure, H is the dimensionless film thickness, L and B are the length and width of a slider bearing, respectively, X and Y are the coordinates along and across the entrainment direction, and $\boldsymbol{\lambda}$ is a vector containing relevant working conditions. The zero pressure boundary condition is implemented at all boundaries of the lubrication area.

A PINN [8, 18] is herein constructed to obtain the solution of the Reynolds equation. Equation (1) is reformulated to $\mathrm{Rey}(N([X,Y]^{\mathrm{T}},\boldsymbol{w});\boldsymbol{\lambda})$ by adopting a neural network ($N([X,Y]^{\mathrm{T}})$, with the weight $\boldsymbol{w}$ and relevant working conditions $\boldsymbol{\lambda}$. The constructed PINN consists of several layers, such as an input layer, a hidden layer, and an output layer (as shown in Fig. 1). X and Y are taken as the inputs, and P is the output. Each layer of a PINN contains several neurons, and the output of each neuron is

$$z=\phi\left(\xi\right) \tag{2}$$

where $\phi(\xi)$ is the activation function, $\xi=w\cdot z'+b$, w is the weight of neuron, z' is the input of the neuron, and b is the bias of the neuron. Here, the sigmoid function is adopted as the activation function:

$$\phi(\xi)=\frac{1}{1+\mathrm{e}^{-\xi}} \tag{3}$$

The loss of PINN is evaluated through the difference between Eq. (1) and the reformulated Reynolds equation across the entire lubrication area:

$$C(\boldsymbol{w})=\iint_{\Omega_{\mathrm{L}}}\left(\mathrm{Rey}(N([X,Y]^{\mathrm{T}};\boldsymbol{w});\boldsymbol{\lambda})-\mathrm{Rey}(P,X,Y;\boldsymbol{\lambda})\right)\mathrm{d}X\mathrm{d}Y \tag{4}$$

where Ω_{L} is the lubrication domain. The minimum value of Eq. (4) can be obtained by the desirable $\boldsymbol{w}$. Equation (4) can be expressed as the sum of losses across the entire lubrication domain and on the boundaries as

$$C(\boldsymbol{w})=\iint_{\Omega_{\mathrm{L}}}\left(f(N([X,Y]^{\mathrm{T}},\boldsymbol{w});\boldsymbol{\lambda})\right)\mathrm{d}X\mathrm{d}Y+\iint_{\partial\Omega_{\mathrm{L}}}\left(b(N([X,Y]^{\mathrm{T}};\boldsymbol{w});\boldsymbol{\lambda})\right)\mathrm{d}X\mathrm{d}Y \tag{5}$$

where $f(N([X,Y]^{\mathrm{T}},\boldsymbol{w});\boldsymbol{\lambda})$ is the difference between $\mathrm{Rey}(N([X,Y]^{\mathrm{T}};\boldsymbol{w});\boldsymbol{\lambda})$ and Eq. (1), $b(N([X,Y]^{\mathrm{T}};\boldsymbol{w});\boldsymbol{\lambda})$ is the boundary condition, and $\partial\Omega_{\mathrm{L}}$ is the lubrication boundary (bearing side edges and inlet/outlet). Equation (5) is readily implemented in relevant PINN solvers, such as Ref. [8]. The PINN in this work is constructed by the *Julia* language as

```
dim = 2
""" input dimension of PINN """
neuron_number = 16
""" neuron number on each layer """
chain = FastChain(FastDense(dim, neuron_number, Flux.σ), FastDense(dim, neuron_number, Flux.σ), FastDense(dim, 1))
```

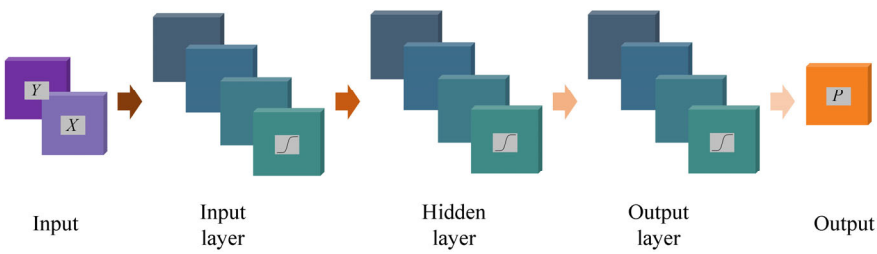

Fig. 1 Illustrative structure of a PINN with three layers.

""" construct a 3-layer PINN, 16 neurons for each layer, activation function for the layer is sigmoid, output (pressure) has 1 dimension """

```
init θ = Float64.(DiffEqFlux.initial_param(chain))
```

""" PINN initialization """

Further detailed instructions on constructing the PINN can be found in Refs. [8, 16].

3 Solution of Reynolds equation by PINN

The pressure distribution is approximated by solving the Reynolds equation (Eq. 1) using PINN. Figure 2 illustrates the hydrodynamic lubrication contact, where the inclined upper surface is static, whilst the lower surface moves with constant velocity U along the X direction. Thus, the entrainment of lubricant results in the hydrodynamic lubrication with the dimensionless film thickness as

$$H(X)=\frac{\theta L}{h_0}(1-X)+1 \tag{6}$$

where θ is the inclination of the slider, and h_0 is the outlet film thickness. We set $\theta=1/1{,}770$, $h_0=3\,\mu\text{m}$, $L=B=4$ mm in the calculation, similar to the working conditions in Ref. [22].

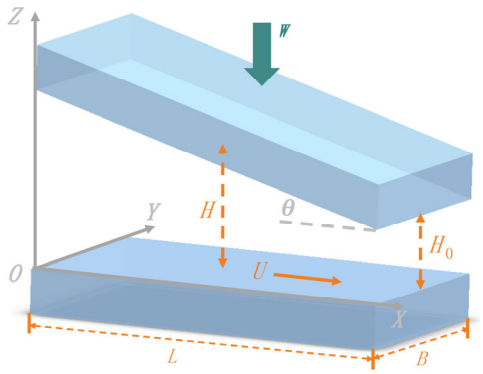

Fig. 2 Illustration of the hydrodynamic lubrication contact.

3.1 Pressure evolution

In contrast with classical methods, PINN trains the neural network by going through a number of epochs before finding the optimal results. Firstly, the evolution of the pressure distribution during the training process is investigated by controlling the maximum allowable epoch number, N_e. It is expected that the results of the PINN training will converge with an epoch number less than N_e. Otherwise, the training will be stopped.

Figure 3 displays the pressure distributions for the first few epochs. Figure 3(a) depicts that the pressure totally deviates from the classical pressure distribution with the first few epochs (small N_e). The peak values of the pressure gradually reduce in Figs. 3(b) and 3(c) during the network training, and the peak pressure

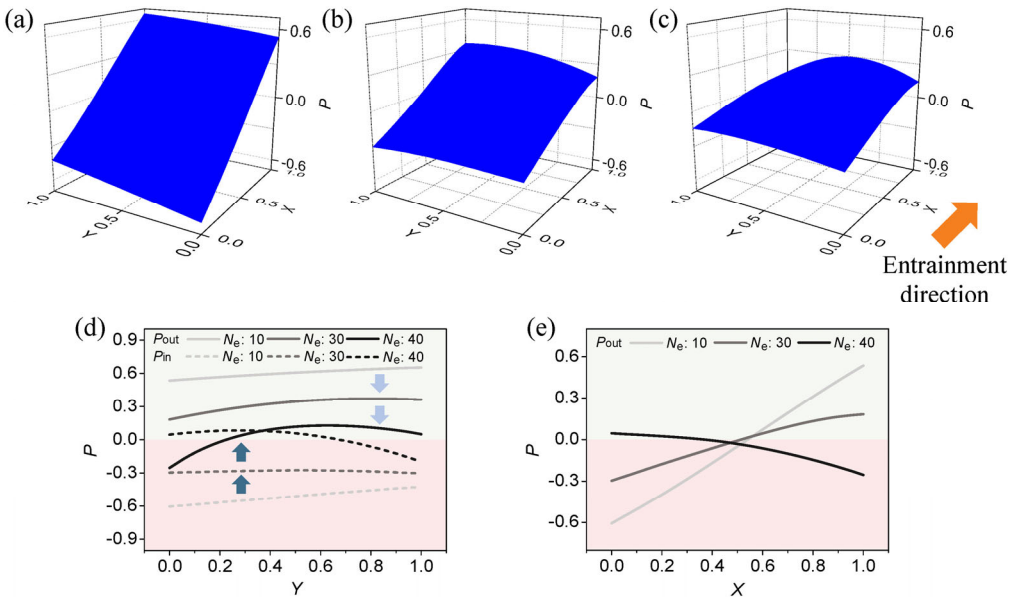

Fig. 3 Calculated pressure distributions for various N_e inside the lubrication domain: (a) N_e = 10, (b) N_e = 30, (c) N_e = 40 and at boundaries, (d) the inlet and outlet, and (e) side edges.

moves towards the central line, $Y = 0.5$. Furthermore, as depicted in Figs. 3(d) and 3(e), the magnitude of the pressure on the boundaries also approaches zero as the network further trains.

Figure 4 indicates that increasing N_e induces the effective convergence of the pressure. Figures 4(a), 4(b), and 4(c) display the pressure distributions for N_e = 100, 500, and 1,000, respectively. Figure 4(a) shows that the pressure distribution calculated with N_e = 100 approaches the conventional shape of the pressure distribution of the hydrodynamic lubrication contacts. However, the pressure on the boundaries greatly deviates from the zero pressure boundary condition. Not only does the pressure distribution further approach conventional results inside the lubrication domain, but also the pressure on the boundaries approaches zero with the further increase in N_e to 500 (Fig. 4(b)) and 1,000 (Fig. 4(c)). Figures 4(d) and 4(e) compare the pressure distributions on the inlet/outlet and side boundaries for N_e = 100, 500, and 1,000 to examine the pressure distribution on the boundaries. The pressure approaches the zero pressure boundary condition best for N_e = 1,000, where the greatest deviation from 0 pressure is approximately 6.8% of the peak pressure.

The convergence of the PINN solution is described by the loss, $C(\boldsymbol{w})$ (Eq. (5)). A typical loss variation during the PINN training process, as shown in Fig. 5(a), indicates that it takes approximately 800 epochs when $C(\boldsymbol{w})$ stabilizes (i.e., the PINN solution

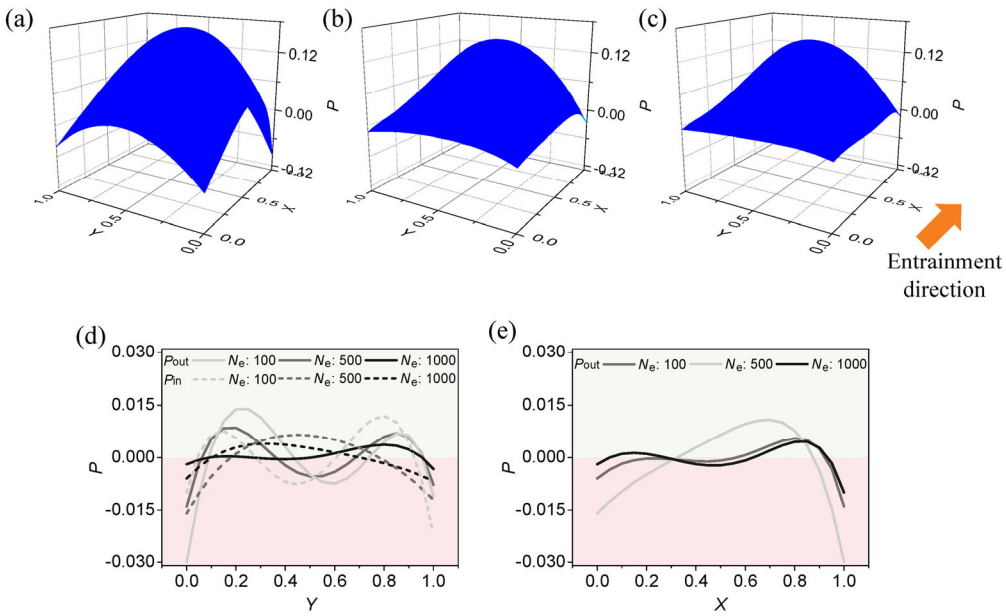

Fig. 4 Convergence of calculated pressures with the increment in N_e. Inside the lubrication domain: (a) N_e = 100, (b) N_e = 500, (c) N_e = 1,000 and at boundaries, (d) the inlet and outlet, and (e) side edges.

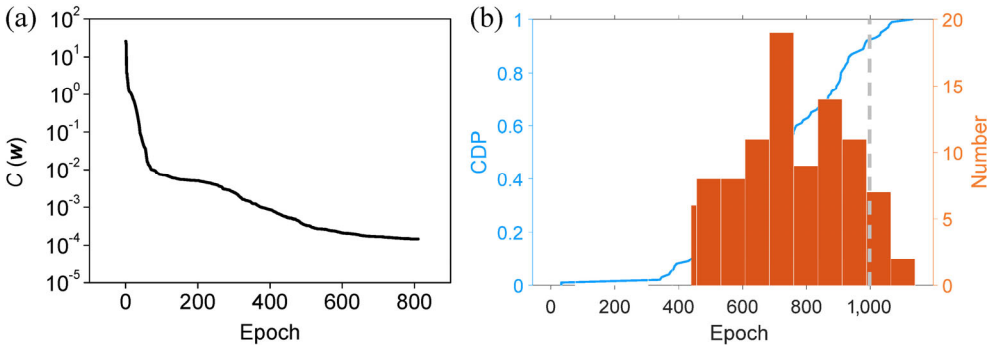

Fig. 5 Training performance. (a) Loss variation during a typical training. (b) Epoch distribution and the epoch's cumulative distribution probability (CDP).

converges). The initial $\boldsymbol{w}$ is randomly generated by the *initial_param*() function in the *DiffEqFlux* package of the *Julia* language during the PINN training. The actual required number of epochs may vary due to different initial $\boldsymbol{w}$ values used in the training process. One hundred independent tests were conducted. The distribution of the required epoch numbers for convergence in these tests and their cumulative distribution probability (CDP) are plotted in Fig. 5(b). Apparently, the probability that the results of PINN training are converged with less than 1,000 epochs is greater than 90%. Thus, N_e = 1,000 is chosen for the following studies. If the results are not converged in 1,000 epochs, they will be discarded and the PINN program will be run again.

The pressure distributions are compared with those calculated by FEM to validate the results obtained by PINN. Figure 6 shows the pressure distributions at Y = 0 (side boundary), Y = 0.25 (1/4 of the total region), and Y = 0.5 (along the central line) obtained by PINN and FEM. The pressure distribution inside the bearing (Y = 0.25 and Y = 0.5) shows excellent correlation of the two methods, and not until near the side boundary does the PINN pressure slightly fluctuate around zero.

3.2 Influence of layer numbers

The effect of the number of hidden layers on the calculation accuracy is investigated. Similar to the neural network configuration provided by Nguyen-Thanh et al. [23], two (1 input and 1 output) to four (1 input, 2 hidden, and 1 output) layers are compared. The comparison of the pressure distributions obtained with two-layer, three-layer, and four-layer PINNs is shown in Fig. 7. They all predict similar pressure distributions inside the lubrication domain. The comparisons of the pressure distributions at the boundary of the three cases and the corresponding peak pressures (0.1490, 0.1446, and 0.1440 for the three cases) show that the pressure results are stabilised with the three-layer PINN (Fig. 7(b)). The four-layer PINN (Fig. 7(c)) does not result in significant improvement on the pressure distributions. The pressure distributions on the side edge (Y = 0) and inlet/outlet boundaries (X = 0 and X = 1) obtained with different layer numbers are plotted in Fig. 8. The results from the two-layer PINN greatly fluctuate from the zero pressure boundary condition. Those from the three-layer and four-layers PINNs approach steady values, and their deviations from zero pressure are not significant. Therefore, the three-layer PINN configuration is adopted in the following studies.

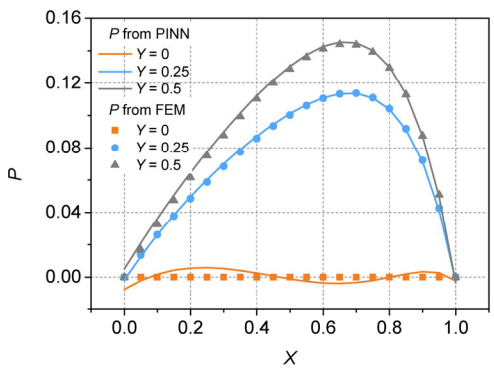

Fig. 6 Comparison of the pressure obtained by PINN and FEM (N_e = 1,000).

3.3 Influence of neuron number

Sixteen neurons for each layer are used in the PINN solution of Eq. (1) in previous sections. However, Nguyen-Thanh et al. [23] used 30 neurons for the hidden layers. Thus, the influence of neuron numbers to the solution accuracy is studied. Figure 9 depicts the pressure distributions obtained by a three-layer PINN with 4, 16, and 32 neurons in each layer (shown in Figs. 9(a), 9(b), and 9(c), respectively). The PINN with four neurons in each layer (Fig. 9(a)) predicts a slightly greater peak pressure. The other two, namely, 16- and 32-neuron PINNs, output similar pressure distributions. The pressures at the bearing boundaries are plotted in Fig. 10. Figures 10(a) and 10(b) depict the pressure distributions at the side edge (Y = 0) and at the inlet/outlet (X = 0 and 1), respectively. The pressures on the boundaries of the four-neuron PINN largely deviate from the zero pressure boundary condition, and the magnitude of deviation is more significant than the other two. The pressure outputs of 16 and 32 neurons (Figs. 9(b) and 9(c)) show similar values. Therefore, the solutions with 16 neurons are converged, and further increment in N_n contributes little to the improvement of solution accuracy.

Therefore, the Reynolds equation can be satisfactory solved by a PINN with 3 layers, 16 neurons for each layer and 1,000 maximum allowable epochs.

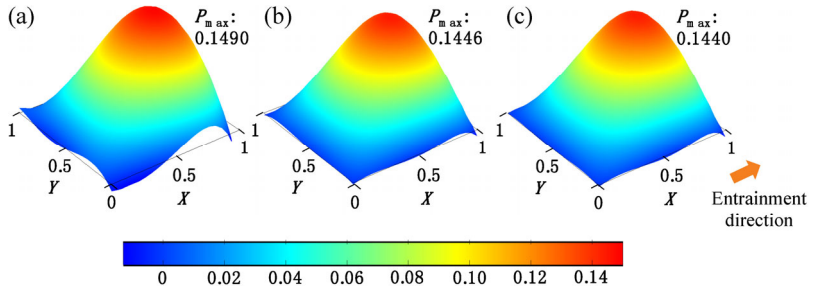

Fig. 7 Pressure distributions with different layer numbers (N_L). (a) $N_L = 2$, (b) $N_L = 3$, (c) $N_L = 4$.

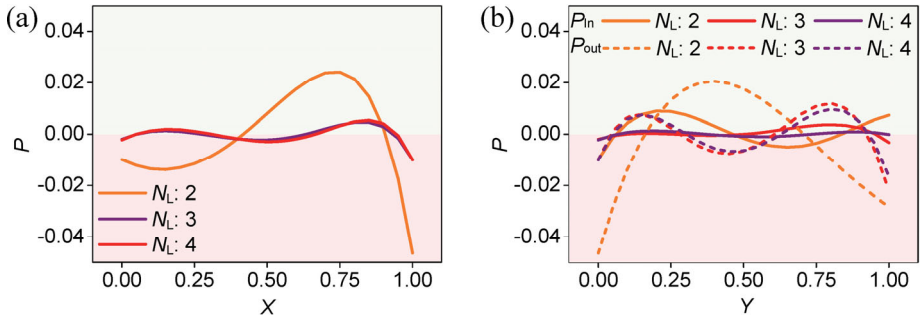

Fig. 8 Pressure distributions at the boundaries. (a) At the side edge. (b) At the inlet and outlet.

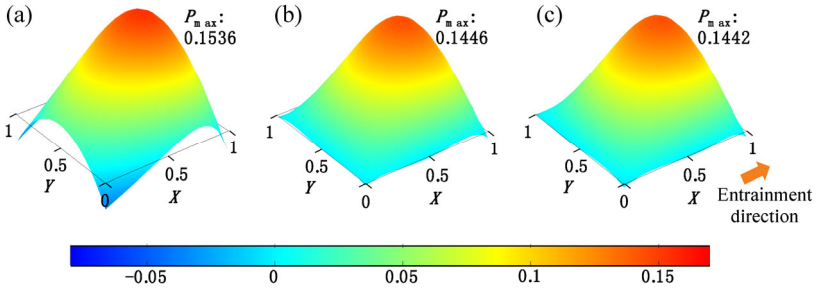

Fig. 9 Pressure distribution with different node numbers per layer. (a) $N_n = 4$, (b) $N_n = 16$, and (c) $N_n = 32$.

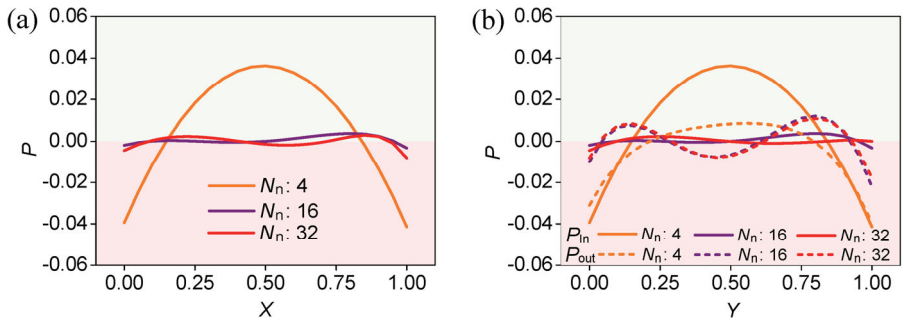

Fig. 10 Pressure distributions at the boundaries. (a) At the side boundary. (b) At the inlet and outlet boundaries.

3.4 Accuracy of PINN

The accuracy of PINN is evaluated in comparison with the conventional FEM. The Reynolds equation is solved based on a given film thickness (at the outlet edge of the slider) of 3 μm and other conditions listed in Table 1.

Table 1 Conditions of the sliding contact.

Static slider surface area	4 mm × 4 mm
Inclination	1/1,770

The PINN model adopts a 3-layer and 16 neurons for each layer structure. The FEM uses the "Weak

Form PDE″ module with the shape function of Lagrange Quadratic in COMSOL 5.3 without any customized algorithm optimization. After obtaining the solutions of the Reynolds equation, i.e., pressure distributions, the load carrying capacity (LCC) can be obtained as

$$\mathrm{LCC} = \Delta x^2 \cdot \sum_{i=1}^{N}\sum_{j=1}^{N}(P_{i,j} + P_{i+1,j} + P_{i,j+1} + P_{i+1,j+1})/4 \quad (7)$$

where the FEM model contains $N \times N$ elements on a $(N+1)\times(N+1)$ grid, Δx^2 is the area of each element. The FEM solutions are obtained with nine different grid sizes, i.e., 20×20, 100×100, 200×200, 300×300, 400×400, 500×500, $1{,}000\times1{,}000$, $1{,}500\times1{,}500$, and $2{,}000\times2{,}000$. With the increase in the number of elements, the FEM results are expected to approach to exact values. While the results of FEM are calculated based on different grid configurations, PINN outputs the pressure distributions of different grids based on only one trained neural network.

The comparisons of PINN and FEM are investigated by the followings:

(1) Relative difference in LCC:

$$\frac{\left|\mathrm{LCC}_{\mathrm{PINN}} - \mathrm{LCC}_{\mathrm{FEM}}\right|}{\mathrm{LCC}_{\mathrm{FEM}}} \quad (8)$$

(2) Maximum pressure difference:

$$\max\left(\left|P^{\mathrm{PINN}} - P^{\mathrm{FEM}}\right|\right) \quad (9)$$

(3) Mean square of the pressure differences:

$$\frac{1}{(N+1)^2}\sqrt{\sum_{i=1}^{N+1}\sum_{j=1}^{N+1}\left(P_{i,j}^{\mathrm{PINN}} - P_{i,j}^{\mathrm{FEM}}\right)^2} \quad (10)$$

(4) Normalized LCC:

$$\frac{\mathrm{LCC}_{\mathrm{FEM}}}{\mathrm{LCC}_{\mathrm{PINN}}} \quad (11)$$

Figure 11(a) shows the relative difference in LCC (Eq. (8)) and the maximum pressure difference (Eq. (9)) of PINN and FEM, which stabilize, respectively, at around 9.2×10^{-3} and 8×10^{-3}. Thus, the differences are less than 1%. Moreover, the mean square of the differences in pressure measured on each node (Eq. (10)) reduces with the increment of number of elements as shown in Fig. 11(b). As the FEM solutions approach to the exact solutions of Reynolds equation with denser grids, the reducing trend of the mean square of pressure differences of PINN and FEM validates the pressure prediction of PINN. Figure 11(c) illustrates that the normalized LCC (Eq. (11))

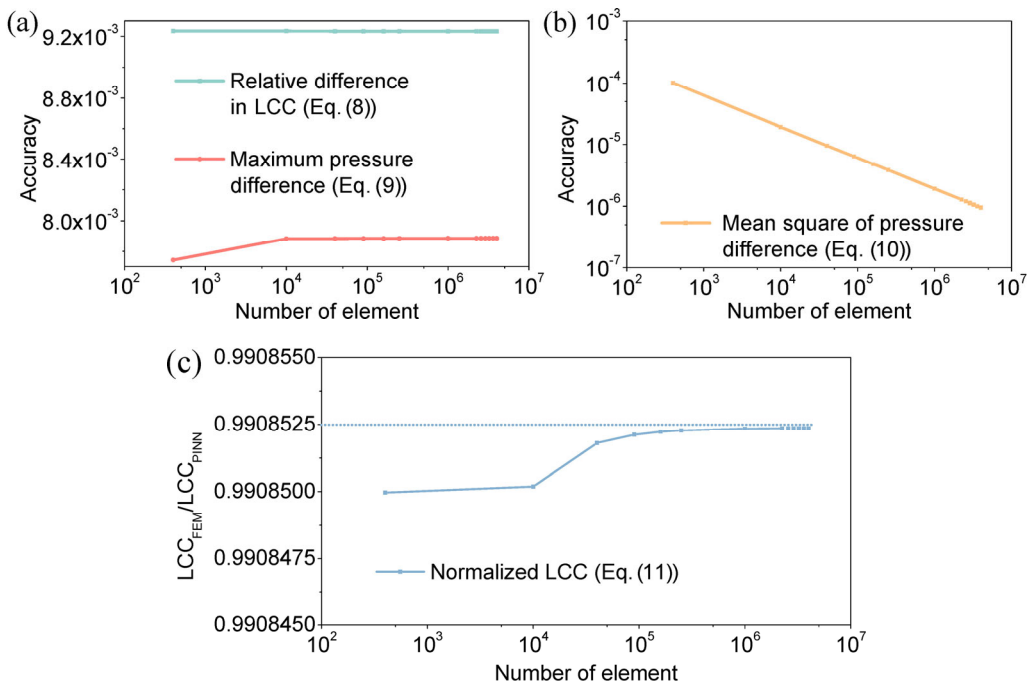

Fig. 11 Comparison between PINN and FEM.

approaches to the steady value of 0.9908525 owing to the reduction in the discretization error in the FEM results by the increase in the number of elements. The steady value represents the exact LCC solution. Thus, the accuracy of PINN is up to 99%, which shows that the developed PINN can accurately calculate both LCC and pressure distributions for hydrodynamic lubrication contacts.

4 Application in the hydrodynamic lubrication contact

The application of the PINN-based method is extended to the analysis of hydrodynamic lubrication. The Reynolds equation is solved by PINN. The converged pressure distribution and the lubricating film thickness, h_0, are deduced through an iterative process (as illustrated in Fig. 12) on the basis of the load balance criterion:

$$\int_{\Omega_L} P(X,Y)\mathrm{d}X\mathrm{d}Y = \frac{Wh_0^2}{\eta UL^2B} \tag{12}$$

where W is the applied load, U is the sliding velocity, and η is the lubricant viscosity.

The developed program is verified by comparing the predicted film thickness with the experimental results [22] measured by optical interferometry [3] on a slider-on-disc test rig. The calculations are based on the operating conditions of the experiment tabulated in Table 2. The FEM calculations are also performed as reference.

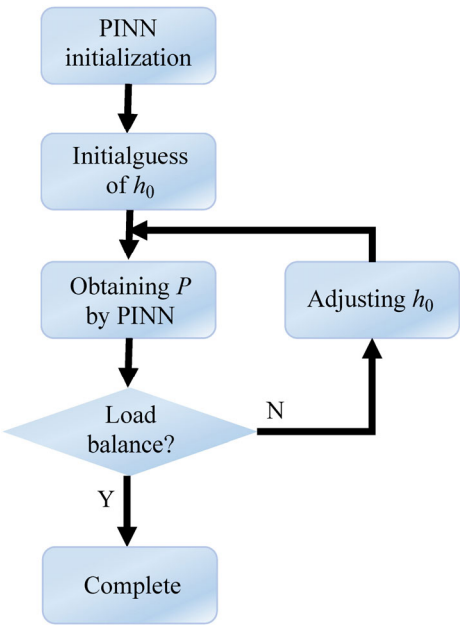

Fig. 12 Flow chart for the hydrodynamic lubrication contact.

The comparisons of the outlet film thickness predicted by PINN and FEM and the experimental measurements are illustrated in Fig. 13. The good correlations amongst the three sets of data, as shown in Fig. 13, prove the effectiveness of the PINN in the calculation of film thickness in the hydrodynamic lubrication contacts.

The pressure distributions obtained by PINN and FEM are compared in Figs. 14 and 15 to further illustrate the accuracy of PINN in the hydrodynamic

Table 2 Experimental condition in Ref. [22].

Static slider surface area	4 mm × 4 mm
Inclination	1/1,770
Bearing load	4 N
Sliding speed	3.7–27.2 mm/s
Dynamic viscosity	0.56 Pa·s

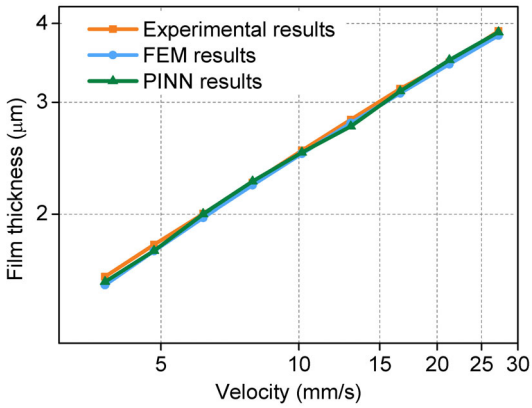

Fig. 13 Outlet film thickness comparison amongst the experimental measurement, FEM calculation, and PINN prediction.

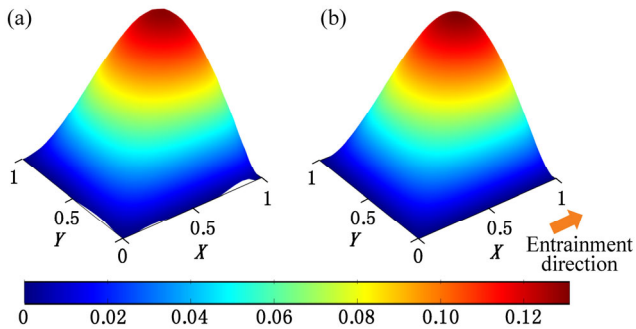

Fig. 14 Calculated pressure distributions (U = 27 mm/s). (a) PINN. (b) FEM.

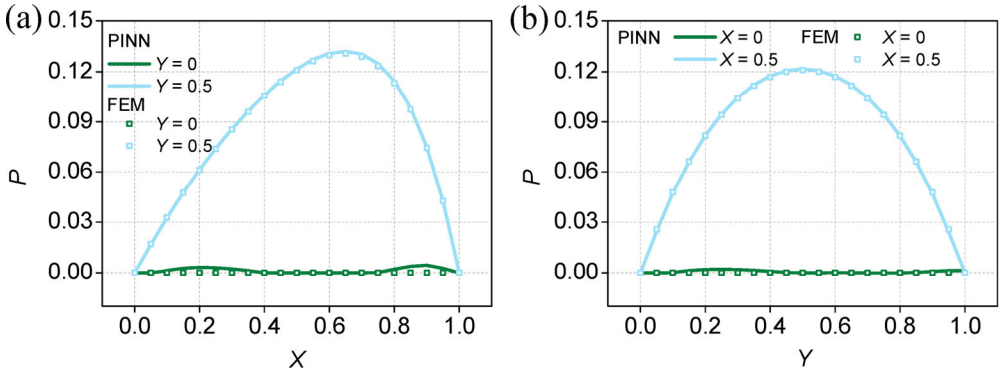

Fig. 15 Pressure comparison between PINN and FEM. (a) Along the entrainment direction. (b) Across the entrainment direction.

lubrication prediction. The PINN and FEM methods output similar pressure distributions inside the hydrodynamic lubrication domain (Fig. 14). Quantitatively, the calculated relative error of PINN in Fig. 14, benchmarked by the FEM result, is only 1.5%. Therefore, the effectiveness of PINN for hydrodynamic lubrication studies is confirmed by such tiny relative error.

The pressure distributions along and across the entrainment direction are depicted in Fig. 15. Although the pressures predicted by PINN at the boundaries (X = 0 and Y = 0) do not strictly satisfy the zero pressure boundary conditions, an excellent correlation between pressure obtained by PINN and FEM prevails in the mid-planes (along X = 0.5 and Y = 0.5). The maximum deviations of pressure at the boundaries from 0 are only 3.4% and 1.7% of the peak pressure in Figs. 15(a) and 15(b), respectively. The film thickness and the pressure distribution comparisons in Figs. 13–15 demonstrate that the PINN method works well in predicting the film thickness and pressure distribution in the hydrodynamic lubrication contact.

The non-zero pressures at the boundaries, as shown in Figs. 14 and 15, can be traced back to the PINN optimization algorithm. When applying PINN to solve the Reynolds equation (Eq. (1)), the target is to find the optimal loss (Eq. (5)) from the pressures inside the computational domain and at the boundaries. Specifically, the network is initialized by the randomly generated weights at the beginning. An optimizer is then adopted to iteratively find the optimal solution until the loss stabilizes. The consideration is based on the governing equation (1st term in Eq. (5)) and the boundary condition (2nd term in Eq. (5)) in the optimization process. Hence, non-zero boundary pressure is allowed as long as the PINN obtains the optimal loss. Different from the PINN method, FEM utilizes a pre-defined grid for the discretization of Eq. (1) and transforms Eq. (1) into a linear algebra problem:

$$\boldsymbol{M}\cdot\boldsymbol{P}=\boldsymbol{F} \tag{13}$$

where the matrix $\boldsymbol{M}$ represents the discretized governing equation, the variable vector $\boldsymbol{P}$ contains both unknown pressure inside the domain and the zero pressure boundary condition, and the vector $\boldsymbol{F}$ indicates the film thickness distribution. The zero pressure boundary condition is *a priori* prescribed in the $\boldsymbol{P}$ vector and in turn, the zero pressure boundary condition must be satisfied.

The information above indicates that PINN could be adopted in lubrication studies for its success in solving the Reynolds equation. With appropriate training algorithm (e.g., *QuadratureTraining* [8]), one can adopt the meshless configuration to solve the Reynolds equation. Conventional numerical methods, such as FEM, rely on the discretization of the Reynolds equation on a pre-defined grid, whereas the PINN algorithm does not require any grid. Although a coarse grid usually works well for hydrodynamic lubrication problems, a dense grid is required in EHL simulations where the computational cost increases greatly. Thus, we envision that the further development of the PINN method could bring benefits in solving complicated lubrication problems.

5 Conclusions

The physics-informed neural network (PINN) has been successfully applied to the analysis of 2D hydrodynamic lubrication. The current work has demonstrated that PINN could achieve satisfactory accuracy in calculating the film thickness and pressure distributions with a structure of 3 layers, 16 neurons per layer, and 1,000 maximum allowable epochs for network training. The results calculated by PINN correlate well with the experimental data and FEM outputs, confirming the application feasibility of PINN in hydrodynamic lubrication studies. As the applicability and efficacy of PINN in solving hydrodynamic lubrication problems are confirmed, PINN has thus the potential to tackle more complicated lubrication problems, such as EHL.

Acknowledgements

This work was supported by the National Natural Science Foundation of China (No. 51805310), the Scientific Research Startup Fund for Shenzhen High-caliber Personnel of SZPT (No. 6022310045k). Special thanks go to Prof. A. Almqvist for his valuable comments on the work.

Author contributions

YZ implemented the PINN codes and drafted the manuscript. LG conducted the experimental measurements and discussed about PINN. PLW contributed mainly on the discussion and presentation.

References

[1] Stachowiak G W. How tribology has been helping us to advance and to survive. *Friction* **5**(3): 233–247 (2017)

[2] Gohar R, Safa M M A. Fluid film lubrication. In *Tribology and Dynamics of Engine and Powertrain.* Amsterdam: Elsevier, 2010: 132–170.

[3] Guo F, Wong P L, Fu Z, Ma C. Interferometry measurement of lubricating films in slider-on-disc contacts. *Tribol Lett* **39**(1): 71–79 (2010)

[4] Nicoletti R. Comparison between a meshless method and the finite difference method for solving the Reynolds equation in finite bearings. *J Tribol* **135**(4): 044501 (2013)

[5] Profito F J, Giacopini M, Zachariadis D C, Dini D. A general finite volume method for the solution of the Reynolds lubrication equation with a mass-conserving cavitation model. *Tribol Lett* **60**(1): 1–21 (2015)

[6] Habchi W, Demirci I, Eyheramendy D, Morales-Espejel G, Vergne P. A finite element approach of thin film lubrication in circular EHD contacts. *Tribol Int* **40**(10–12): 1466–1473 (2007)

[7] Habchi W. Reduced order finite element model for elastohydrodynamic lubrication: Circular contacts. *Tribol Int* **71**: 98–108 (2014)

[8] Zubov K, McCarthy Z, Ma Y, Calisto F, Pagliarino V, Azeglio S, Rackauckas C. NeuralPDE: Automating physics-informed neural networks (PINNs) with error approximations. *arXiv preprint* arXiv: 2107.09443 (2021)

[9] Pandiyan V, Prost J, Vorlaufer G, Varga M, Wasmer K. Identification of abnormal tribological regimes using a microphone and semi-supervised machine-learning algorithm. *Friction* **10**(4): 583–596 (2022)

[10] Meng Y G, Xu J, Jin Z M, Prakash B, Hu Y Z. A review of recent advances in tribology. *Friction* **8**(2): 221–300 (2020)

[11] Rosenkranz A, Marian M, Profito F J, Aragon N, Shah R. The use of artificial intelligence in tribology—A perspective. *Lubricants* **9**(1): 2 (2021)

[12] Zhang Z, Yin N, Chen S, Liu C. Tribo-informatics: concept, architecture, and case study. *Friction* **9**(3): 642–655 (2021)

[13] Canbulut F, Yildirim Ş, Sinanoğlu C. Design of an artificial neural network for analysis of frictional power loss of hydrostatic slipper bearings. *Tribol Lett* **17**(4): 887–899 (2004)

[14] Perčić M, Zelenika S, Mezić I. Artificial intelligence-based predictive model of nanoscale friction using experimental data. *Friction* **9**(6): 1726–1748 (2021)

[15] Sadegh H, Mehdi A N, Mehdi A. Classification of acoustic emission signals generated from journal bearing at different lubrication conditions based on wavelet analysis in combination with artificial neural network and genetic algorithm. *Tribol Int* **95**: 426–434 (2016)

[16] Raissi M, Perdikaris P, Karniadakis G E. Physics-informed neural networks: A deep learning framework for solving forward and inverse problems involving nonlinear partial differential equations. *J Comput Phys* **378**: 686–707 (2019)

[17] Hornik K, Stinchcombe M, White H. Multilayer feedforward networks are universal approximators. *Neural Netw* **2**(5): 359–366 (1989)

[18] Samaniego E, Anitescu C, Goswami S, Nguyen-Thanh V M, Guo H, Hamdia K, Zhuang X, Rabczuk T. An energy approach to the solution of partial differential equations in computational mechanics via machine learning: Concepts, implementation and applications. *Comput Methods Appl Mech Eng* **362**: 112790 (2020)

[19] Nguyen-Thanh V M, Anitescu C, Alajlan N, Rabczuk T, Zhuang X Y. Parametric deep energy approach for elasticity accounting for strain gradient effects. *Comput Methods Appl Mech Eng* **386**: 114096 (2021)

[20] Almqvist A. Fundamentals of physics-informed neural networks applied to solve the Reynolds boundary value problem. *Lubricants* **9**(8): 82 (2021)

[21] Bach F. Breaking the curse of dimensionality with convex neural networks. *J Mach Learn Res* **18**(1): 629–681 (2017)

[22] Guo L, Wong P L, Guo F. Boundary yield stress and interfacial potential energy barrier in thin film hydrodynamic lubrication. *Tribol Lett* **62**(1): 1–8 (2016)

[23] Nguyen-Thanh V M, Zhuang X, Rabczuk T. A deep energy method for finite deformation hyperelasticity. *Eur J Mech A Solids* **80**: 103874 (2020)

Yang ZHAO. He obtained his Ph.D. degree from both City University of Hong Kong and Xi'an Jiaotong University in 2019, and his B.S. degree from China University of Mining and Technology in 2013. He is currently a lecturer in Shenzhen Polytechnic. His research interests include lubrication, computational tribology, and interfacial phenomena.